

Chapter 2

Brittle and Ductile Fracture

This chapter is devoted to damage and fracture micromechanisms operating in the case when monotonically increasing forces are applied to engineering materials and components. According to the amount of plastic deformation involved in these processes, the fracture events can be categorized as brittle, quasi-brittle or ductile.

Brittle fracture is typical for ceramic materials, where plastic deformation is strongly limited across extended ranges of deformation rates and temperatures. In polycrystalline ceramics the reasons lie in a high Peierls–Nabarro stress of dislocations due to strong and directional covalent bonds (this holds also for some ionic compounds), and in less than five independent slip systems in ionic crystals (e.g., [149]). In amorphous ceramics it is simply because of a lack of any dislocations and, simultaneously, strong covalent and ionic interatomic bonds. Metallic materials or polymers exhibit brittle fracture only under conditions of extremely high deformation rates, very low temperatures or extreme impurity concentrations at grain boundaries. In the case of a strong corrosion assistance, brittle fracture can also occur at very small loading rates or even at a constant loading (stress corrosion cracking). A typical micromechanism of brittle fracture is so-called cleavage, where the atoms are gradually separated by tearing along the fracture plane in a very fast way (comparable to the speed of sound). During the last 50 years, the resistance to unstable crack initiation and growth, i.e., the fracture toughness, became a very efficient measure of brittleness or ductility of materials. In the case of cleavage, this quantity can be simply understood in a multiscale context. The macroscopic (continuum) linear–elastic fracture mechanics (LEFM) developed by Griffith and Irwin brought to light an important relationship between the crack driving force G (the energy drop related to unit area of a new surface) and the stress intensity factor K_I as

$$G = \frac{1 - \nu^2}{E} K_I^2.$$

This relation holds for a straight front of an ideally flat crack under conditions of both the remote mode I loading and the plane strain. The energy necessary for creation of new fracture surfaces can be supplied from the elastic energy drop of the cracked solid and/or from the work done by external forces (or the drop in the associated potential energy). Thus, at the moment of unstable fracture, the Griffith criterion gives $G_c \approx 2\gamma$, where γ is the surface (or fracture) energy that represents a resistance to cleavage. Consequently

$$\gamma \approx \frac{1 - \nu^2}{2E} K_{Ic}^2. \quad (2.1)$$

However, the surface energy can be expressed also in terms of the cohesive (bonding) energy needed to break down an ideal crystal or an amorphous solid into individual atoms. The bonding energy of a surface atom is a half of that associated with an internal atom [150] and, because of two fracture surfaces, one can simply write

$$\gamma = \frac{U}{4S}, \quad (2.2)$$

where U is the cohesive energy assigned to one atom and S is the area per atom on the fracture surface. With regard to Equations 2.1 and 2.2 it reads

$$K_{Ic} \approx \left(\frac{EU}{2S} \right)^{1/2}. \quad (2.3)$$

Values of U can be calculated either *ab initio* or by using semi-empirical interatomic potentials (see the previous chapter), and they can also be experimentally determined as twice the sublimation energy. For most metallic and ceramic crystals, values of U and S are in units of eV/atom and 10^{-19} m^2 , respectively. Thus, according to Equation 2.3, values of fracture toughness in the case of an ideal brittle fracture are as low as $K_{Ic} \in (0.5, 1) \text{ MPa m}^{1/2}$. This range represents a lower-bound physical benchmark for the fracture toughness of engineering materials, and it corresponds well to experimental results achieved in tests with classical ceramic materials such as glasses or porcelain. Similar considerations can also be applied to classical ceramic materials that do not contain macroscopic pre-cracks. Indeed, some pores or microcracks are always present in such materials.

In advanced ceramic materials for engineering applications, however, the level of fracture toughness is substantially enhanced. This can be achieved by microstructurally induced crack tortuosity combined with the presence of many small particles (or even microcracks) around the crack front. In this way the crack tip becomes shielded from the external stress supply and the stress intensity factor at the crack tip reduces. Both the theoretical background and the practical example of that technology are discussed in Section 2.1 in more details. Another method, commonly utilized for an additional improvement of fracture toughness of ceramics, is the distribution of supplied energy to

damage mechanisms other than pure cleavage. This can be succeeded, for example, by an enforcement of phase transformations in the vicinity of the advancing crack front [149].

In cracked metallic solids, however, the measured values of K_{Ic} are at least an order of magnitude higher than the lower-bound benchmark. This holds even for ferrite (bcc Fe) at very low temperatures, where almost microscopically smooth cleavage fractures along $\{001\}$ planes appear (note that the $\langle 001 \rangle$ direction in Fe is associated with the lowest ideal tensile strength). The value of related fracture energy was experimentally found to be about 14 Jm^{-2} [149]. This means that the energy supplied for the unstable fracture is also considered here for the development of localized plastic deformation around the crack tip. Hence, the general thermodynamic criterion for unstable crack growth [19] can be written in the Griffith–Orowan form

$$\frac{1 - \nu^2}{E} K^2 \geq 2\gamma + w_p(K, \gamma), \quad (2.4)$$

where $w_p(K, \gamma)$ is the plastic work needed for building the plastic zone at the crack tip. While this work can be neglected in the case of brittle fracture, it is of the same order of magnitude as 2γ in the case of quasi-brittle fracture in metals. Note that the crack tip emission of dislocations in metals already occurs at very low K values in units of $\text{MPa m}^{1/2}$ (see Section 3.2 for more details). The dislocations emitted from the crack tip generate an opposite stress intensity factor so that the crack tip becomes shielded from increasing external (remote) loading. The plastic work consumption proceeds until the moment when the sum of external and internal stress intensity factors at the crack tip (the local K -factor) exceeds the critical value necessary for separating atoms to produce new surfaces in an unstable (cleavage) manner [151,152]. This is mathematically expressed in Equation 2.4 so that the plastic work $w_p(K, \gamma)$ is written as a function of both γ and K . Thus, the moment of cleavage fracture is somewhat delayed and, as reported by many authors [153–155], a short stage of stable crack growth often precedes the unstable propagation. The microstructurally induced heterogeneity in the resistance to both the unstable crack growth (γ) and the dislocation emission can, sometimes, produce a series of elementary advances and arrests of the crack tip.

Many quasi-brittle fractures in practice occur as a consequence of pre-existing corrosion dimples, large inclusions or fatigue cracks. However, the localized plastic deformation at favourable sites in the bulk also enables the creation of microcracks as nucleators of the quasi-brittle fracture in solids which do not contain any preliminary defects. At phase or grain boundaries it can be accomplished by many different and well known micromechanisms conditioned by the existence of high stress concentrations in front of dislocation pile-ups. Let us briefly mention another mechanism of crack initiation in bcc metals first introduced by Cottrell [156]. When two edge dislocation pile-ups are driven by the applied stress σ and meet on different $\{110\}$ glide

planes in the grain interior, their interaction results in the nucleation of a [001] sessile dislocation. This dislocation can be considered to be a wedge in the {001} cleavage plane. Interaction of n dislocations of Burgers vector b then creates a microcrack with flank opening nb . The work $W = \sigma n^2 b^2$ done by the force σnb acting at the front of n dislocations along the distance nb must be equal to the energy $2\gamma nb$ for the creation of new crack surfaces. This gives the microscopic criterion for quasi-brittle fracture as

$$\sigma_c nb = 2\gamma_s, \quad (2.5)$$

where σ_c is the critical (fracture) stress. Assuming the relation connecting the number of dislocations with the grain size d in terms of the Hall–Petch relation, Equation 2.5 can be rearranged to

$$(\sigma_0 \sqrt{d} + k_y) k_y = \beta G \gamma_s, \quad (2.6)$$

where σ_0 is the yield stress, k_y constant in the Hall–Petch relation (temperature dependent), β the temperature independent constant and G the shear modulus (weakly temperature dependent). Thus, the right-hand side of Equation 2.6 is practically independent of temperature. If the left-hand side is equal to or higher than the right-hand side, the brittle (or quasi-brittle) fracture initiates just at the moment of reaching the yield stress. In an opposite case, the ductile failure occurs after some deformation hardening period. Both the high deformation rate and the low temperature enhance σ_0 as well as k_y , thereby giving rise to quasi-brittle fracture. The same is caused by a large grain size. Thus, the criterion at Equation 2.6 correctly predicts the experimentally observed fracture behaviour. Note that this simple model for single-phase bcc metals is of a two-level type, since the Hall–Petch relation can be easily interpreted by combined atomistic-dislocation considerations [149].

In Section 2.2 a statistical approach to geometrical shielding effects occurring in multi-phase engineering materials is outlined. This two-level concept can be used to give quantitative interpretation of some rather surprising results obtained when measuring the fracture toughness and the absorbed impact energy (notch toughness) of some metallic materials. Examples of such interpretation are documented for ultra-high-strength low-alloyed (UHSLA) steels and Fe-V-P alloys.

Unlike brittle or quasi-brittle fracture, the ductile fracture starts with a rather long period of stable crack or void growth due to the bulk plastic deformation. In the case of pre-cracked solids this means that the surface energy 2γ becomes negligible when compared to the plastic term $w_p(K, \gamma)$ in Equation 2.4, and this criterion loses its sense. Therefore, instead of stress-based criteria (fracture stress, critical stress intensity factor) the deformation-based criteria are more appropriate for a quantitative description of ductile fracture. In the first stage of ductile fracture, microvoids (micropores) nucleate preferentially at the interface between the matrix and secondary phase particles.

The physical reasons are clear: high interfacial energy (low fracture energy), the incompatibility strains (dislocation pile-ups) and the mosaic stresses induced by a difference in thermal dilatations of the matrix and inclusions. Nucleated voids experience their stable growth controlled by the plastic deformation. In the tensile test, for example, the voids become cylindrically prolonged by uniaxial deformation up to the moment when the ultimate strength is reached. Beyond that limit they also expand in transverse directions under the triaxial state of stress inside the volume of developing macroscopic neck.

Although the bulk ductile fracture occurs only very exceptionally in engineering practice, the research of that process is important for forging technologies. Besides the two-scale analysis of plastic deformation, some models of void coalescence during the tensile test are outlined in the last section of this chapter. It should be emphasized that the damage process inside the crack-tip plastic zone of many metallic materials can also be described in terms of the ductile fracture mechanism (e.g., [157]). Therefore, an analytical model that enables a prediction of fracture toughness values by means of more easily measurable ductile characteristics is also presented.

2.1 Brittle Fracture

From the historical point of view, brittle fracture proved to be one of the most frequent and dangerous failures occurring in engineering practice. Besides the well known brittleness of utility ceramics and glasses, metallic materials may also exhibit intrinsically brittle properties dependent on temperature; there exists a critical temperature, the so-called ductile-brittle transition temperature (DBTT) under which the material is brittle, while it is ductile above that temperature. This holds particularly for bcc metals, in which cores of screw dislocation are split into sessile configurations [4, 158]. They remain immobile at low temperatures so that, under such conditions, cleavage is a dominant fracture mechanism. However, a steep exponential increase of ductility appears when approaching the DBTT owing to thermal activation helping to increase the mobility of screw segments. Improper application of a material below this temperature can have catastrophic consequences, such as, for example, the sinking of the RMS Titanic nearly one hundred years ago. The material of Titanic, although representing the best-grade steel at that time, was characterized by coarsened grain and high level of inclusions so that DBTT was higher than 32°C. No wonder this ship was catastrophically destroyed by brittle fracture during its impact with the iceberg at the water temperature of -2°C [159].

However, brittleness is often induced by other effects such as flawed material processing or segregation of deleterious impurities at grain boundaries. Grain boundary segregation can result in a local enrichment of thin but continuous interfacial layers throughout the polycrystalline material with con-

centrations as much as several orders of magnitude higher than that in the grain interior [160]. The most dangerous impurities segregating in bcc iron and steels are phosphorus, tin and antimony. For example, the disintegration of the rotor at the Hinkley Point Power Station turbine generator in 1969 was caused by 50% of phosphorus segregated at grain boundaries of the 3Cr1/2Mo low-alloy steel containing a few tenths of a percent of phosphorus in the bulk [161].

Brittle intercrystalline (intergranular) decohesion caused by impurity segregation exhibits relatively high microroughness of fracture surfaces. Moreover, the secondary cracks identifying the splitting of the main crack front are often observed preferentially at triple points. Both these phenomena lead to the so-called geometrically induced shielding (GIS) of the crack tip that has a favourable effect on decreasing the local stress intensity factor, thereby increasing the fracture toughness. This kind of shielding is one of the so-called extrinsic components of fracture toughness that can be considered as a possible toughening mechanism in the research and technology of advanced materials.

In the next subsections, the theory of GIS and its practical application to an improvement of fracture toughness of brittle materials is outlined.

2.1.1 Geometrically Induced Crack Tip Shielding

Crack front interactions with secondary-phase particles or grain (phase) boundaries in the matrix structure cause deflections of the crack front from the straight growth direction resulting in the microscopic tortuosity of cracks. As already mentioned, such waviness combined with crack branching (splitting) is a natural property of intergranular cracks in metals as well as ceramics. In general, the tortuosity induces a local mixed-mode I+II+III at the crack front even when only a pure remote mode I loading is applied. In order to describe the crack stability under mixed-mode loading, various LEFM-based criteria were proposed (see, e.g., [162–164]). Several of the most frequently used mixed-mode criteria can be found in Appendix B, where conditions of their validity are also briefly described. When selecting a suitable criterion one should note that an unstable brittle fracture in metallic materials is usually preceded by a stable corrosion and/or fatigue crack growth to some critical crack size. During such growth the crack always turns perpendicularly to the direction of maximal principal stress, i.e., to the opening mode I loading. This physically corresponds to minimization of both the crack closure (see Chapter 3 for more details) and the friction so that the rough crack flanks behind the tortuous crack front do not experience any significant sliding contact. Because the crack-wake friction is responsible for somewhat higher fracture toughness values measured under remote sliding modes II and III when compared to those under mode I [164], one can consider an approx-

imate equality $K_{Ic} \approx K_{IIc} \approx K_{IIIc}$ along tortuous crack fronts of remote mode I cracks. Moreover, first unstable pop-ins at these fronts follow, most probably, the local planes of already pre-cracked facets. Consequently, the simplest stability criterion

$$G_{eff} = G_I + G_{II} + G_{III},$$

can be accepted, where G_{eff} is the effective crack driving force. An almost equivalent relation is often used in terms of stress intensity factors:

$$K_{eff} = \sqrt{K_I^2 + K_{II}^2 + \frac{1}{1-\nu} K_{III}^2}. \quad (2.7)$$

For example, in the case of a long straight crack with an elementary kinked tip, it simply reads

$$K_{eff} = \cos^2(\theta/2) K_I, \quad (2.8)$$

where θ is the kink angle. One can clearly see that $K_{eff} < K_I$ for $\theta > 0$. This inequality generally holds for any spatially complex crack front. Hence, the local stress intensity K_{eff} at such a front is always lower than the remote K_I -factor applied to a straight (smooth) crack of the same macroscopic length. The geometrically induced shielding (GIS) effect belongs, according to Ritchie [165], to so-called extrinsic shielding mechanisms. The resistance to crack propagation in fracture and fatigue has, in general, many components that can be divided into two main categories: intrinsic and extrinsic toughening. The first mechanism represents the inherent matrix resistance in terms of the atomic bond strength or the global rigidity, strength and ductility. Appropriate modifications to both the chemical composition and the heat treatment are typical technological ways to improve the intrinsic fracture toughness. On the other hand, processes like kinking, meandering or branching of the crack front, induced mostly by microstructural heterogeneities, belong typically to the extrinsic toughening mechanisms. They reduce the crack driving force and, apparently, increase the intrinsic resistance to crack growth. Thus, the measured fracture toughness can be expressed as a sum of the intrinsic toughness and extrinsic components:

$$K_{Ic} = K_{Ici} + \sum K_{Ice}. \quad (2.9)$$

The standardized procedure for calculation of K_{Ic} -values [166] assumes a planar crack with a straight front and, therefore, does not take the extrinsic shielding effect associated with the crack microgeometry into account. Hence, surprisingly high K_{Ic} -values might be measured, particularly for materials with coarse microstructures and highly tortuous cracks. General expressions for GIS contributions in both brittle and quasi-brittle fracture were derived in [167, 168] by following the approach first introduced by Faber and Evans [169]. In the case of brittle fracture

$$K_{Ici} = \left(\frac{\bar{g}_{eff,r}}{R_A} \right)^{1/2} K_{Ic}, \quad (2.10)$$

where K_{Ic} and K_{Ici} are respectively the measured (nominal) and intrinsic values of fracture toughness, $\bar{g}_{eff,r}^{1/2} = \bar{k}_{eff,r}$ is the mean effective k -factor for the tortuous crack front, normalized to the remote K_I ($k_{eff,r} = K_{eff}/K_I$), and R_A is the area roughness of the fracture surface. Equation 2.10 can be derived by the following simple reasoning.

Let us consider a cracked body of a thickness B with an intrinsic resistance G_{Ici} against the crack growth under remote mode I loading. The coordinate system x, y, z is related to the crack front in the usual manner (Figure 2.1). The straight crack front with no geometrical shielding (GIS) represents a trivial case. Here, obviously, the measured fracture toughness value G_{Ic} (or K_{Ic}) is equal to its intrinsic value, i.e., $G_{Ic} \equiv G_{Ici}$ (or $K_{Ic} \equiv K_{Ici}$).

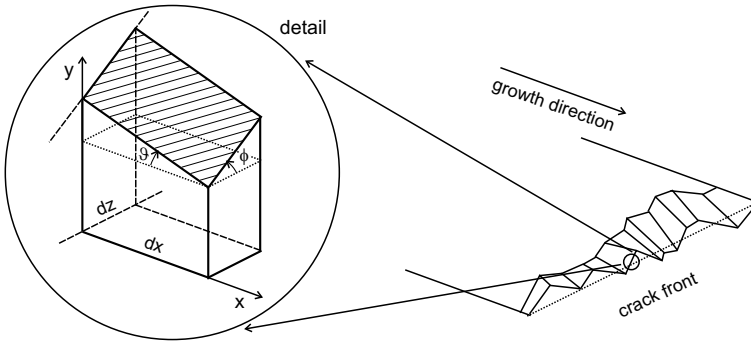


Figure 2.1 Scheme of the tortuous crack front and its segment. Reprinted with permission from John Wiley & Sons, Inc. (see page 265)

When the crack front is microscopically tortuous, a variable local mixed-mode 1+2+3 characterized by g_{eff} or k_{eff} values is present generally at each site along the crack front. During the external loading under increasing remote value G_I , the proportionality $g_{eff} \sim G_I$ or $k_{eff} \sim K_I$ must be valid. Thus, the ratio $g_{eff,r} = g_{eff}/G_I$ can be introduced as independent of G_I but dependent on the crack front tortuosity. Let G_{uI} be the remote crack driving force at the moment of an unstable elementary extension dx of the crack front. This value is equal to the conventionally measured (nominal) fracture toughness G_{Ic} . Then the nominal elementary energy release rate due to the creation of a new crack surface area $dx dz$ is equal to $G_{uI} dx dz$. However, the actual (local) elementary energy release rate at the tortuous crack front is

$$g_{eff} dx dz = g_{eff,r} G_{uI} dx dz.$$

Consequently, the total energy available for the creation of a new surface area Bdx along the crack front can be written as

$$dW = G_{uI} dx \int_0^B g_{eff,r} dz. \quad (2.11)$$

As follows from Figure 2.1, however, the real new elementary surface area $dS = R_A B dx$ is greater than $B dx$ since

$$R_A = \frac{1}{B} \int_0^B \frac{dz}{\cos \phi(z) \cos \vartheta(z)}. \quad (2.12)$$

In Equation 2.12, R_A is the roughness of the fracture surface and $dx dz / (\cos \phi \cos \vartheta)$ is the area of the hatched rectangle in Figure 2.1. Because G_{Ici} is the intrinsic resistance to crack growth, the total fracture energy must be

$$dW = G_{Ici} dS = G_{Ici} R_A B dx. \quad (2.13)$$

Combining Equations 2.11 and 2.13 and denoting

$$\bar{g}_{eff,r} = \frac{1}{B} \int_0^B g_{eff,r} dz,$$

one obtains

$$G_{uI} \equiv G_{Ic} = \frac{R_A}{\bar{g}_{eff,r}} G_{Ici}. \quad (2.14)$$

In general, $G_{Ic} \geq G_{Ici}$ since $\bar{g}_{eff,r} \leq 1$ and $R_A \geq 1$. Therefore, the nominally measured fracture toughness G_{Ic} is usually higher than the intrinsic (real) matrix resistance G_{Ici} . According to the relation $G_{Ic}/G_{Ici} = (K_{Ic}/K_{Ici})^2$, Equation 2.14 can be eventually rewritten to obtain Equation 2.10.

Values of $\bar{g}_{eff,r}$ and R_A must be estimated by using numerical (or approximate analytical) models of the real tortuous crack front combined with appropriate experimental methods for fracture surface roughness determination. In Sections 2.1.2 and 2.1.3, the so-called pyramidal- and particle-induced models are presented. In the context of 2D crack models, the tortuosity is usually described by a double- or even single-kink geometry and $R_A = 1/\cos \theta$ is assumed. In the 2D single kink approximation at Equation 2.8, the crack front is assumed to be straight ($R_A = 1$). Consequently, Equation 2.10 takes the following form:

$$K_{Ici} = \cos^2(\theta/2) K_{Ic}.$$

Besides both the kinking and the meandering, the crack branching can also take place especially in the case of intergranular fracture. This process causes further reduction of SIF ahead of the crack tip and, therefore, Equation 2.10 is to be further modified. According to [170], the crack branching reduces the local SIF approximately to one half of its original magnitude. Let us denote A_b the area fraction of the fracture surface influenced by crack branching. When accepting a linear mixed rule, Equation 2.10 can be then modified as

$$K_{Ici} = \left(\left(\frac{\bar{g}_{eff,r}}{R_A} \right)^{1/2} (1 - A_b) + 0.5A_b \right) K_{Ic}. \quad (2.15)$$

The area A_b can be determined by measuring the number of secondary cracks (branches) occurring on fracture profiles prepared by polishing metallographical samples perpendicular to the fracture surface [171] (see also Section 3.2). Twice the sum of projected lengths of branches into the main crack path divided by the true crack length yields a plausible estimate of A_b .

When omitting the crack branching and considering Equations 2.9 and 2.10, the extrinsic GIS component of fracture toughness can be simply expressed as $K_{Ice} = (1 - \sqrt{\bar{g}_{eff,r}/R_A}) K_{Ic}$. Brittle fracture in metallic materials occurs only when a pure cleavage or intergranular decohesion takes place. In these cases the extrinsic components other than geometrical (such as zone shielding or bridging) can be neglected. In the particular case of cleavage fracture (bcc metals at very low temperatures) one usually observes that $R_A < 1.2$ and $\bar{g}_{eff,r} > 0.9$. This means that GIS is rather insignificant. On the other hand, the extrinsic component K_{Ice} might be very high when the intergranular fracture cannot be avoided (strong corrosion or hydrogen assistance, grain-boundary segregation of impurities and tempering embrittlement of high-strength steels). In that case, however, the favourable effect of the extrinsic component is usually totally destroyed by an extreme reduction of the intrinsic component K_{Ici} . Nevertheless, one can still improve the fracture toughness of both metals and ceramics by increasing the extrinsic (shielding) component without the loss of general quality in mechanical properties (see Sections 2.1.2, 2.2.2 and 3.2.6).

2.1.2 Pyramidal Model of Tortuous Crack Front

A plausible assessment of the GIS effect is possible only when the following steps can be realized:

1. building of a realistic model of the crack front based on a 3D determination of fracture surface roughness;
2. calculation of local normalized stress intensity factors k_{1r} , k_{2r} and k_{3r} along the crack front;
3. calculation of the effective stress intensity factor $k_{eff,r}$.

The first step can be achieved by the 3D reconstruction of fracture morphology. The second problem can be solved, for example, by using the software package FRANC3D based on the boundary element method [172]. The third step is solvable by standard mathematics. A nearly exact numerical solution by means of the FRANC3D code is, however, usually extremely time consuming. Therefore, a simple pyramidal model of the crack front was proposed for approximate analytical estimations [168, 173]. This model is based on a pyramid-like periodic approximation of the tortuous crack front, each element of which is characterized by the twist angle Φ and the highest tilt angle Θ_m towards the macroscopic crack plane; see Figure 2.2.

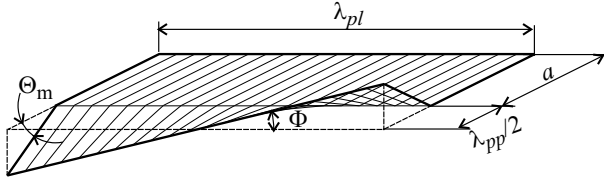


Figure 2.2 A periodic element of the pyramidal model of tortuous crack front

The profile roughness R_L (measured along the crack front) and the periodicity λ_{pl} (λ_{pp}) measured parallel (perpendicular) to the crack front are associated with the angles Φ and Θ_m by the following simple equations:

$$\lambda_{pp} \tan \Theta_m = \lambda_{pl} \tan \Phi, \quad R_L = \cos^{-1} \Phi. \quad (2.16)$$

The characteristic periodicities λ_{pl} and λ_{pp} can be determined either by the Fourier analysis of roughness profiles measured at appropriate locations on the fracture surface, or simply identified with a characteristic microstructural periodicity, e.g., with the mean grain size. The effective stress intensity factor $k_{eff,r}$ (normalized to the remote K_I factor) at each point of the pyramidal front can be calculated by using Equation 2.7 with the following approximate analytical expressions for local stress intensity factors:

$$\begin{aligned} k_{1r} &= \cos \left(\frac{\Theta}{2} \right) \left[2\nu \sin^2 \Phi + \cos^2 \left(\frac{\Theta}{2} \right) \cos^2 \Phi \right], \\ k_{2r} &= \sin \left(\frac{\Theta}{2} \right) \cos^2 \left(\frac{\Theta}{2} \right), \\ k_{3r} &= \cos \left(\frac{\Theta}{2} \right) \sin \Phi \cos \Phi \left[2\nu - \cos^2 \left(\frac{\Theta}{2} \right) \right]. \end{aligned} \quad (2.17)$$

The results calculated according to Equation 2.17 are sufficiently accurate provided that $\lambda_{pp} \ll 2a$, where a is the pre-crack length. The global effective factor $\bar{k}_{eff,r}$, averaged for the periodic crack front geometry composed of identical pyramidal elements, can then be computed as

$$\bar{k}_{eff,r} = \frac{\pi - 2}{2\Theta_m(2R_L + \pi - 4)} \int_{-\Theta_m}^{\Theta_m} \left(k_{1r}^2 + k_{2r}^2 + \frac{k_{3r}^2}{1 - \nu} \right) d\Theta. \quad (2.18)$$

Comparison of results obtained by means of the pyramidal model and the FRANC3D code revealed that, in the whole range of both the surface roughness and the roughness periodicity typical for real intergranular surfaces, the difference lies within the 10% of error band [168]. Although the pyramidal model yields very promising results predominantly in the case of intercrystalline fracture (see Section 2.2.2), it can also be quite successfully applied to other brittle fracture modes, as shown in the next section.

2.1.3 Fracture Toughness of Particle Reinforced Glass Composite

Traditional ceramic materials such as glass or porcelain possess amorphous microstructures. An absence of crystallographically conditioned dislocations makes these materials extremely brittle. However, the very low intrinsic fracture toughness of glass in the range $K_{Ici} \in (0.5, 1) \text{ MPa m}^{1/2}$ may be improved, for example, by reinforcing with second constituents with high modulus, high strength and/or high ductility in the form of fibres, whiskers, platelets or particulates embedded into the matrix [174, 175]. A successful example of ceramic platelet reinforcement of glass is the borosilicate glass/ Al_2O_3 platelet composite that was first introduced by Boccaccini *et al.* [176]. Based on this system, environmentally friendly and cost-effective materials can be produced as alumina platelets for the building industry or as abrasives for the polishing industry. The enhancement in fracture toughness can be ascribed here to four concurrent phenomena [176–180]: the Young's modulus increment resulting from the platelets addition (the intrinsic component), the presence of a compressive residual stress in the glass matrix, the crack tip shielding produced by platelets and the crack deflection mechanism (extrinsic components). The shielding effect is a result of local mixed-mode I+II+III induced by rigid particles surrounding the crack tip. The crack deflection is forced particularly by a necessity to bypass rigid particles when searching the direction of the highest crack driving force (compare Section 2.2.1). This leads to a zig-zag crack propagation in between the platelets (crack tortuosity) and a reduction of the crack driving force in comparison to that of the straight crack. This must be associated with an enhanced microroughness of fracture surfaces. A direct correlation between the roughness of the fracture surface and the fracture toughness of dispersion reinforced ceramic and glass composites has been suggested and experimen-

tally proved [180–182]. Because these systems provide an excellent possibility to verify theoretical GIS models, quantitative assessments of all the above-mentioned intrinsic and extrinsic effects have been performed [183,184]. Moreover, extended experimental analysis of fracture toughness, fracture surface roughness and microstructure was performed on samples made of borosilicate glass containing different volume fractions of alumina platelets.

2.1.3.1 Experimental Procedure and Results

The experimental glass matrix composite was fabricated via powder technology and hot pressing. Alumina platelets of a hexagonal shape, with major axes between $5 - 25\ \mu\text{m}$ and axial ratio of 0.2, were used. The commercially available borosilicate glass was selected for the composite matrix. The microstructure of specimens containing 0, 5, 10, 15 and 30 vol.% of platelets [176] consisted of a dense glass matrix with a more or less homogeneous distribution of platelets. A strong bond between the matrix and the platelets was confirmed by transmission electron microscopy [185]. Upon cooling from the processing temperature, the thermal expansion mismatch between matrix and reinforcement induces tangential compressive and radial tensile residual stress in the matrix around the particles. Fracture toughness values were obtained using test pieces of a standard cross-section ($3 \times 4\ \text{mm}^2$) with the chevron notch machined by an ultra thin diamond blade. A Zwick/Roell electromechanical testing machine was utilized for the three-point bending test with a span of 20 mm. Scanning electron microscopy (SEM) was used for the fractographic analyses of fracture surfaces. Roughness parameters were measured by the optical profilometer MicroProf FRT based on a chromatic aberration of its lens. The device works with vertical resolution of 3 nm and lateral resolution of about $1\ \mu\text{m}$. A three-dimensional reconstruction of surface topography was performed by means of the software Mark III. The surface roughness was quantified by the average area roughness, R_A , defined on the basis of the ISO 4278 norm as the arithmetic mean of the deviations of the roughness profile from the central line. The profile roughness R_L , defined in a standard manner as the true profile length divided by its projected length, was also determined. The profiles obtained from 3D fracture surface morphology quantification were subjected to Fourier analysis in order to determine the characteristic periodicities λ_{pp} and λ_{pl} . The measured values for all specimens are displayed in Table 2.1.

Note that values of λ_{pp} are an order of magnitude lower than the double-length of the pre-crack ($2a = 4\ \text{mm}$) which ensures a reasonable validity of the pyramidal model.

Dependencies of both the relative area roughness $R_r = R_A(X\%)/R_A(0\%)$ and the average fracture toughness on different alumina platelet volume contents (X%) are shown in Figure 2.3. It is seen that both curves increase linearly with increasing content of alumina platelets in the matrix approx-

Table 2.1 Characteristics of the pyramidal model related to tortuous cracks in measured specimens

Al ₂ O ₃ (vol.%)	R _L	λ _{pp} [μm]	λ _{pl} [μm]	Θ _m	$\bar{k}_{eff,r}$
0	1.011	373	114	0.0455	0.983
5	1.053	412	171	0.3178	0.924
10	1.199	102	32	0.2040	0.763
15	1.115	341	170	0.2410	0.719
30	1.229	102	128	0.7311	0.714

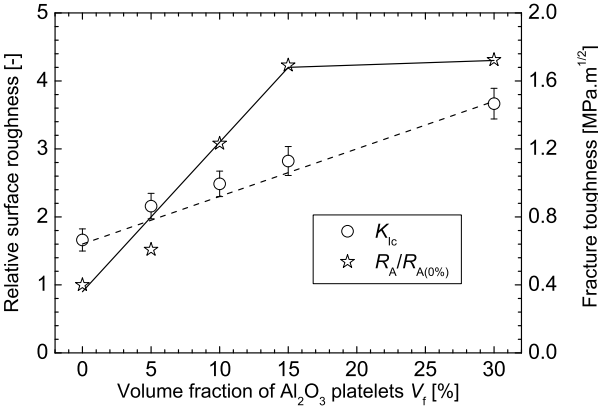


Figure 2.3 Dependence of the relative surface roughness and the fracture toughness on the volume content of alumina platelets in the glass matrix. Reprinted with permission from Elsevier B.V. (see page 265)

imately up to $X = 15\%$. The increase in roughness is, unlike that of the fracture toughness, effectively stopped at higher platelet contents. This also means that other mechanism(s) should be acting to counteract the loss of effectiveness of crack deflection here. Typical examples of reconstructed fracture surfaces obtained from the profilometric measurement for both 0 and 30 vol% of alumina platelets are depicted in Figure 2.4. It is evident that the fracture surface roughness was significantly increased when alumina platelets were incorporated into the borosilicate glass matrix.

At the highest volume fraction of alumina platelets (30 vol%), however, platelet clusters are already observed as shown in Figure 2.5. It seems to be plausible that the crack front interacts with the whole cluster rather than with all its individual platelets. Thus, some particles inside clusters do not directly contribute to the crack front deflection (the surface roughness).

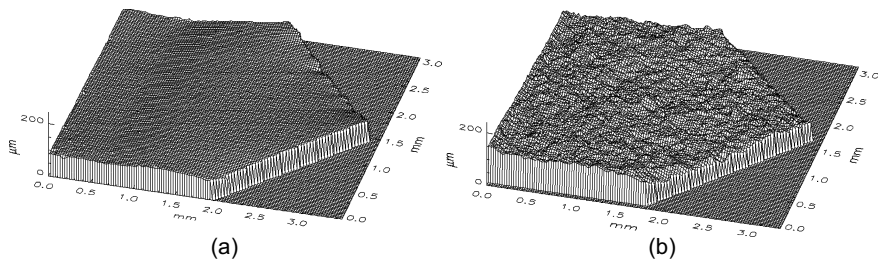


Figure 2.4 Three-dimensional reconstructed fracture surfaces for 0 and 30 vol% of alumina platelets. Reprinted with permission from Elsevier B.V. (see page 265)

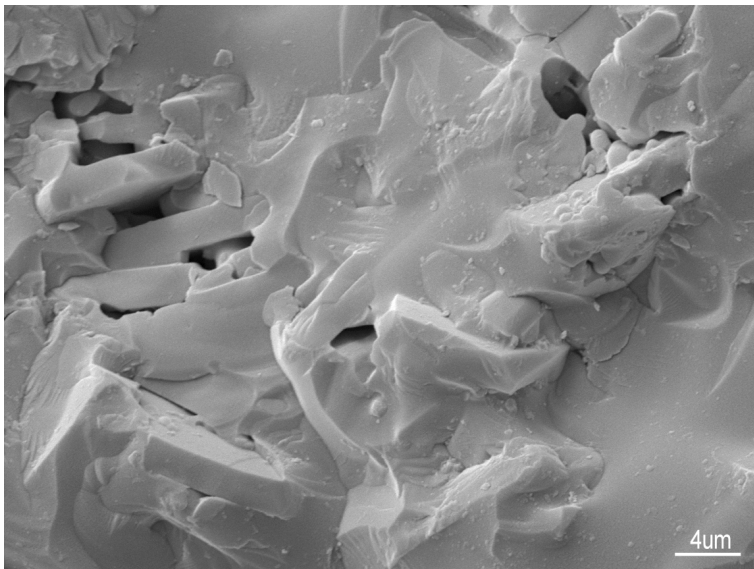


Figure 2.5 Clusters of platelets in the sample with 30% reinforcement volume. Reprinted with permission from Elsevier B.V. (see page 265)

2.1.3.2 Theoretical Assessment of the Shielding Effect

Besides the roughness-induced shielding (RIS), the crack tip shielding caused by surrounding rigid particles has to also be considered. This effect can be approximately assessed according to results reported in [178,183]. In these works, the shielding effect produced by rigid circular particles was analyzed in the frame of the 2D ANSYS model based on the finite element method. The presence of such inclusions generally induces the mixed-mode I+II at the tip of the straight crack.

The rigid particles possessed 20 times higher Young's modulus than the matrix. Particles of different sizes (diameter $d = 6, 12, 30, 60, 120, 240 \mu\text{m}$),

spaced by $l = 30, 60, 90, 120 \mu\text{m}$, were considered. Moreover, geometrically identical particles of negligibly small moduli (holes) were also studied for comparative reasons. Note that the range $d/l \in (0.1, 3)$ corresponds to the particle volume fraction $f_p \in (0.04, 25)\%$. Several thousands of possible positions of the crack tip were analyzed within an investigated area in between a pair of spherical particles, according to the scheme in Figure 2.6. This area was long enough to incorporate the influence of further neighbouring pairs of particles (behind and ahead of the investigated area, dashed lined) which were not explicitly considered in the analysis.

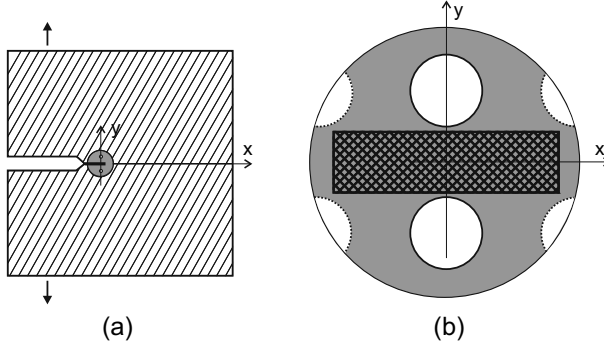


Figure 2.6 The scheme related to the model of particle-induced crack tip shielding: (a) position of the investigated region in the testing sample, and (b) detail of the region (*black rectangle*) and circular particles

This enabled us to generalize the results to a periodic square network of particles by multiplication of normalized effective SIFs in the points which lie within both the left-hand and the right-hand parts of the investigated region and are associated owing to the translation periodicity.

The effective SIF ($k_{eff,r} = \sqrt{k_{I,r}^2 + k_{II,r}^2}$) was used to assess the effective crack driving force. Averaged values of \bar{k}_{eff} as functions of the ratio d/l for all analyzed types of particles are displayed in Figure 2.7. One can see that the rigid inclusions start to produce some shielding after reaching the critical value $(d/l)_c = 0.2$ (or $f_{pc} = 0.5\%$). Then the normalized effective k -factor rather slowly drops to the value of 0.9 that corresponds to $(d/l) = 3$ (or $f_p = 25\%$). Practically the same decrease was identified in the case of holes. Here, however, the drop was shifted to a higher critical value $(d/l)_c = 1$ (or $f_{pc} = 6.5\%$). Despite this rather slight difference, the shielding effect of both rigid particles and holes appeared to be similar.

In order to assess the RIS, the pyramidal model was applied in the first approximation by using the roughness characteristics from Table 2.1. The dependence of the relative fracture toughness $K_{Ic}(X\%)/K_{Ic}(0\%)$ (where $K_{Ic}(0\%) = K_{Ici} = K_{Icm}$), calculated using Equations 2.16, 2.17 and 2.18, on the volume fraction of Al_2O_3 platelets is plotted by the dashed line in

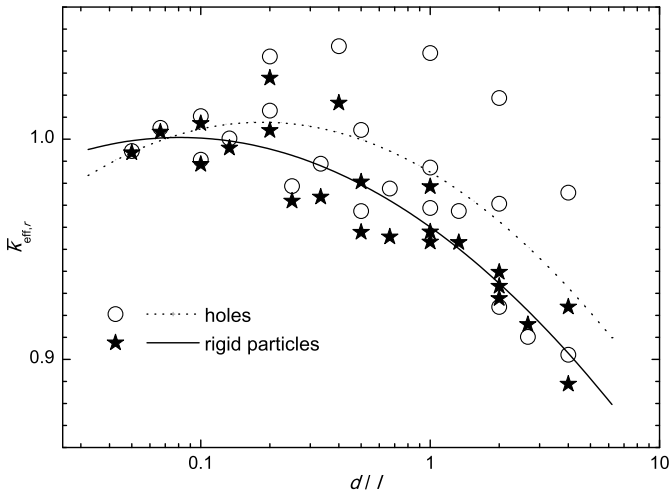


Figure 2.7 Averaged values of the effective stress intensity factor as a function of the particle size/spacing ratio for all analyzed types of particles

Figure 2.8 along with the experimental data. As expected, the maximal predicted relative increase of 40% in the fracture toughness cannot fully explain the real improvement of 120% that was achieved by the 30% volume fraction of platelets.

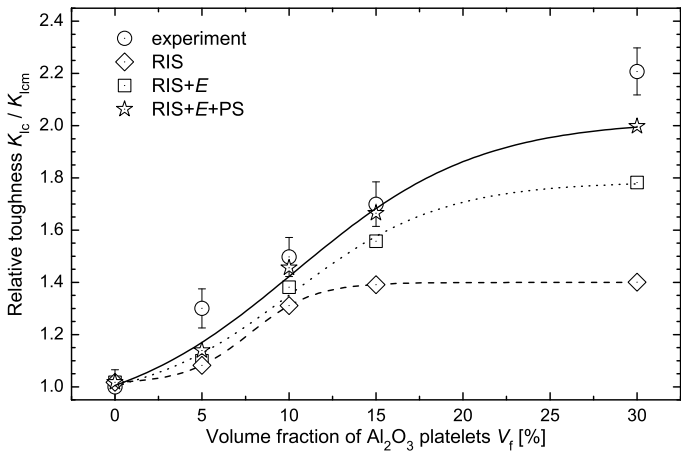


Figure 2.8 Theoretical curves of the relative fracture toughness as functions of the percentage of Al_2O_3 particles in comparison with experimental data. The *full line* shows the theoretical prediction including all considered corrections

Indeed, one must also consider the decrease in the crack driving force related to both the increase in Young's modulus and the shielding induced by platelets [177]. The increase in fracture toughness due to the increase in Young's modulus can be calculated from

$$\frac{K_{Ic}}{K_{Icm}} = \sqrt{\frac{E}{E_m} \frac{G_c}{G_{Icm}}}, \quad (2.19)$$

where E is Young's modulus of the composite and $E_m = E(0\%)$ is Young's modulus of the matrix, the values of which are given in Table 2.2 [176]. The improved prediction (RIS+ E) including this effect is shown by the dotted line in Figure 2.8.

Because the difference in shielding produced by rigid particles and holes was found to be negligible, one can use the result plotted in Figure 2.7 as a further correction of the theoretical curve. By considering the relevant volume fractions of experimental samples (the value $\bar{k}_{eff,r} = 0.9$ was used for $X = 30\%$), the final theoretical prediction (RIS+ E +PS) is shown by the full line in Figure 2.8.

Table 2.2 Young's moduli of borosilicate glass matrix composite containing different volume fractions of Al_2O_3 platelets

Platelets content [vol.%]	E [GPa]
0	63
5	65
10	70
15	79
30	102

One can see that the agreement between theory and experiment is reasonable.

A somewhat more complex and exact model was proposed by Kotoul *et al.* [184]. This model considered several additional toughening mechanisms, such as compressive residual stresses or crack front trapping at platelets that may be effective in these composites. Moreover, it could explain the experimental fact that the fracture roughness ceased to increase from about 15vol% of Al_2O_3 . The model follows from the theory of particle-induced crack deflection that was developed by Faber and Evans. However, some errors in the expression for the strain energy release rate, appearing in their original paper [169], had to be corrected. After relevant modification, the following equation for the normalized effective crack driving force was obtained:

$$\begin{aligned}
g_{eff,r} = & \cos^2 \frac{\lambda}{2} \left(2\nu \sin^2 \phi + \cos^2 \frac{\lambda}{2} \right)^2 \cos^4 \phi + \\
& + \cos^2 \phi \sin^2 \frac{\lambda}{2} \cos^4 \frac{\lambda}{2} + \\
& + \frac{\cos^2 \frac{\lambda}{2} \sin^2 \phi \cos^2 \phi}{1 - \nu} \left(2\nu - \cos^2 \frac{\lambda}{2} \right)^2.
\end{aligned} \tag{2.20}$$

Here Θ is a tilt angle and Φ is a twist angle of crack front elements induced by their interaction with platelets. Note that Equation 2.20 possesses the required limiting properties, i.e.,

$$\lim_{\phi \rightarrow \pi/2} g_{eff,r} \rightarrow 0, \quad \lim_{\phi \rightarrow 0} g_{eff,r} \rightarrow \cos^4 \frac{\theta}{2}$$

which was not the case in the originally derived expressions in [169]. Details concerning the calculation of the averaged crack driving force $\bar{g}_{eff,r}$ can be found elsewhere [184]. This solution also involves the contribution of the change in Young's modulus according to Equation 2.19. The theoretical prediction was in very good agreement with experimental data. This result revealed that, most probably, the contributions of residual stresses as well as crack trapping could be negligible. Indeed, as shown in [184], the presence of high residual radial tensile stresses along the platelet circumference leads to crack front propagation around the particle to relieve these stresses (no crack trapping). Simultaneously, however, the segment of the crack front propagating through the matrix is shortened and the corresponding twist angle decreases which results in flattening of the crack front in the matrix. This raises the energy release rate $\bar{g}_{eff,r}$ and makes it easier for the crack propagation in the tangential compressive stress field within the matrix. As a result, the net toughening increment given by $\bar{g}_{eff,r}$ remains unchanged and the residual stress contribution also does not take any effect.

Taking the above-mentioned considerations into account, the peculiar occurrence of a plateau in the plot of fracture surface roughness as a function of platelet volume fraction (Figure 2.3) can also be elucidated. There are two contributions to the surface roughness related to (1) crack propagation around the platelets and (2) crack propagation within the matrix. The former grows with increasing platelet concentration. The latter decreases with increasing platelets concentration because the fracture surface in the matrix flattens. Moreover, due to clustering of platelets, their vicinity becomes less effective at deflecting cracks and, as a result, the corresponding contribution to the surface roughness further decreases. Beyond about 15% volume fraction of platelets, the positive and the negative contributions to the surface roughness mutually compensate and the increase in surface roughness stops.

In summary, one can say that the models based on coupled shielding effects are able to elucidate quantitatively the increase in fracture toughness caused by particle reinforcement of glass-based ceramics.

2.2 Quasi-brittle Fracture

Microscopically smooth cleavage cracks, observed in ferrite at very low temperatures, possess the surface energy of 14 Jm^{-2} which is much higher than that of about 1 Jm^{-2} related to the lower-bound benchmark for ideal cleavage cracks. A satisfactory explanation gives the cleavage mechanism based on alternative short-range dislocation slip proposed by Knott [186]. A pair of $(1/2)\langle 111 \rangle (1\bar{1}0)$ and $(1/2)\langle 1\bar{1}\bar{1} \rangle (110)$ edge dislocations are emitted from the cleavage crack front $[010]$ to a distance of several Burgers vectors to produce an elementary crack advance in $[100]$ direction. After that advance the dislocations immediately disappear on newly created surfaces as a consequence of attractive mirror forces. In this way, microscopically flat fracture surfaces with neither slip markings nor dislocations in their vicinity might be produced. The fracture energy associated with that process can be assessed as 12 Jm^{-2} which is close to the above-mentioned experimental value.

However, this kind of perfectly smooth cleavage crack is the exception rather than the rule. The cleavage fracture in metallic materials is, even at low temperatures, usually accompanied by clear microscopic traces of local plastic deformation. The so-called steps, tongues and fishbones are produced by interaction of the crack front with dislocation tangles or twins [187]. The most typical morphological features are so-called river markings that are created by shear connections of steps originating at grain boundaries with non-zero twist component. They are enforced by a necessity of gradual re-initiation of the cleavage crack when penetrating to a twisted cleavage plane in the adjacent grain (see Figure 2.9). In metallic materials, therefore, at least a small plastic zone at the crack tip is always to be expected. Even in the case of intergranular fracture along strongly weakened grain boundaries, at least several percent of cleavage and/or dimple fracture facets are always present on the fracture surface. This experimental observation was proven by a theoretical model [188] showing that a pure intergranular crack front would, during its advance, require higher tortuosity and more spatial geometrical complexity [189]. This would demand a steadily increasing fracture energy to a unit projective area. Consequently, at rather early crack growth stages, the cleavage of some of the largest grains becomes more energetically favourable than their intergranular decohesion. Thus, the fracture morphology of quasi-brittle cracks consists of a mixture of intergranular facets (microscopically tortuous) and transgranular cleavage or dimple facets (microscopically nearly straight). The intergranular, cleavage and dimple fractures represent brittle, quasi-brittle and ductile components of the fracture process, respectively. Thus, in spite of a macroscopically brittle appearance, the fracture processes in metallic materials are to be considered as quasi-brittle.

It is well known that LEFM can be successfully used for the description of quasi-brittle fracture only when the plastic zone size

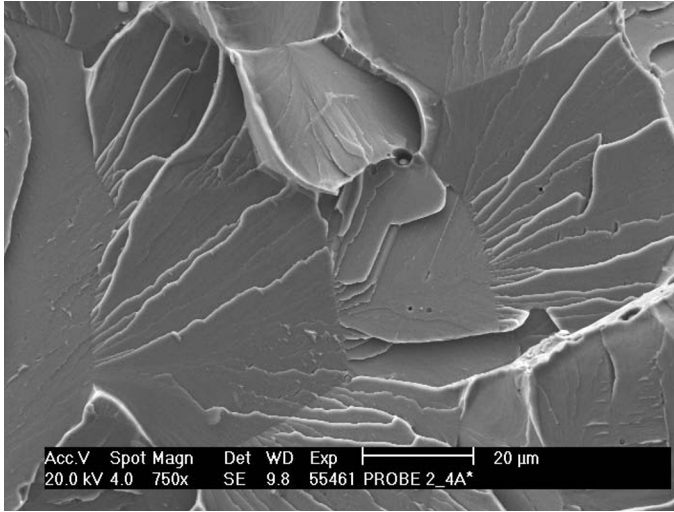


Figure 2.9 A typical picture of river markings on cleavage facets (mild steel)

$$r_p = \frac{1}{\xi} \left(\frac{K}{\sigma_y} \right)^2, \quad (2.21)$$

where $\xi \approx 2\pi$, is very small in comparison to the crack length a and the thickness B of the component. Under such conditions of small-scale yielding and plane strain the laboratory tests of fracture toughness K_{Ic} remain more or less invariant with respect to both the specimen shape and the crack location. Indeed, the elastic-plastic stress-strain behaviour of even very ductile materials becomes quasi-brittle inside the small plastic zone (see Section 2.3.2). When also taking the constraint effect into account, which means comparable values of T-stress (the second term in the Williams expansion) depending on the ligament w between the crack tip and the free surface of the specimen and the component, the K_{Ic} values obtained in the laboratory tests can be more safely transferred to large engineering components [190, 191]. However, the plastic zone size is also an important quantity with respect to the microscopic mode of crack propagation that is affected by materials microstructure. In that respect, naturally, it should be related to a characteristic microstructural distance d , e.g., to the grain (particle) size or interparticle (interphase) spacing. Such a parameter is called the size ratio. Similarly to the brittle fracture case shown in Section 2.1, the microscopic mode of crack propagation might also have a strong impact on the resistance to unstable crack growth in the case of quasi-brittle failures. In this connection, the size ratio plays a very important role. This will be demonstrated in the next subsections in a theoretical as well as an experimental manner.

2.2.1 Statistical Approach to Geometrical Shielding Based on Size Ratio Effect

A lot of experimental evidence about the special role of the size ratio $S_R = d/r_p$ was collected during the last three decades of fracture and fatigue research. Hitherto, only the mean values d_m or $S_{Rm} = d_m/r_p$ were usually taken into consideration. Numerous experiments [192–194] revealed that the crack path is particularly influenced by microstructure (grain boundaries, phase boundaries, precipitates, inclusions) when the plastic zone size is comparable to or smaller than the mean characteristic microstructural distance, i.e., when $S_{Rm} \geq 1$. Microscopically tortuous, intergranular or crystallographic fracture morphology is predominantly observed under these circumstances. On the other hand, the crack path becomes insensitive to microstructure when the plastic zone size embraces many microstructural elements, i.e., when $S_{Rm} \ll 1$. In this case, ductile dimples or non-crystallographic quasi-cleavage are observed on rather smooth and straight transgranular fracture surfaces. In fatigue, many authors [195–197] reported the maximum percentage of intergranular facets at those sites of the fracture surface, where the cyclic plastic zone size was exactly equal to the mean grain size ($S_{Rm} \approx 1$).

The theory of yield stress gradient effects in inhomogeneous materials (e.g., [198]) or the discrete dislocation models in fatigue (e.g., [199]) yield a general basis for elucidation of the above-mentioned phenomena. According to the former theory, the interaction between the crack tip and the near-inhomogeneous region becomes significant only when $S_{Rm} \geq 1$. Following this interaction, the crack will either circumvent high-strength heterogeneity or deflect to the low-strength one. Similarly, the discrete dislocation models reproduce well the strong interaction of crack tip with grain boundaries when the crack tip plasticity is constrained within one or a small number of grains. Once the plastic zone size becomes much higher than the mean grain size, the interaction effects decay and the crack growth rate starts to be quite unaffected by the microstructure. The maximum of intergranular morphology at $S_{Rm} \approx 1$ in fatigue can be explained by considering intergranular (or interfacial) misfit strains [168]. If the above condition holds, grains of the mean size closely adjacent to the fatigue crack front become, unlike their neighbours (more distant to the crack front), cyclically plastically deformed. The related cyclic mismatch stresses at boundaries between neighbouring grains can preferentially lead to intergranular (or interphase) relaxation cracking. Due to only slightly asymmetric Weibull (or log-normal) probability density of the grain size in metallic materials [200–202], the grain sizes close to the average are the most probable ones. Thus, the large strain mismatch causing intergranular fracture becomes most probable just when the condition $S_{Rm} \approx 1$ becomes fulfilled at the advancing fatigue crack front.

In most engineering materials, the scatter of both the grain size and the particle spacing causes variation of the parameter d within more than two

orders of magnitude along the crack front. On the other hand, a sharp decrease of the stress with distance from the crack front leads to localization of the plastic deformation within a narrow zone of approximately constant width along the whole crack front. Therefore, the plastic zone size follows the Hall–Petch rule in terms of the mean grain size and the yield stress [203], and remains rather invariable along the crack front with the exception of plane stress regions close to free specimen surfaces. As a consequence, the size ratio S_R follows the grain size distribution and varies in a wide range along the crack front inside the specimen. In other words, there are many sites at the crack front where $S_{Rm} \ll 1$ or $S_{Rm} \geq 1$ is to be expected. However, only the latter locations contribute to the microscopic tortuosity that induces GIS, while the effect of the former ones can be neglected. Therefore, the statistical approach seems to be the most relevant way to describe the GIS effect in quasi-brittle materials.

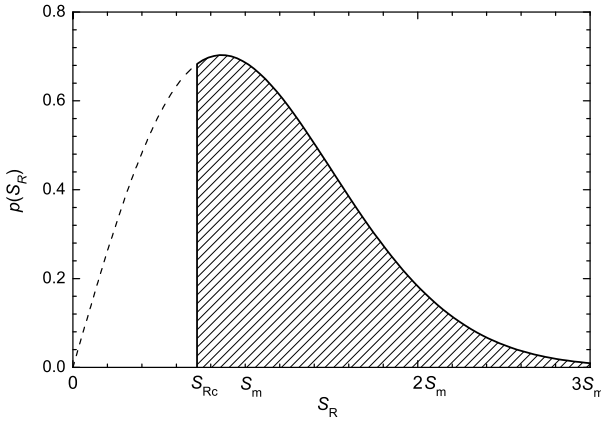


Figure 2.10 Probability density function $p(S_R)$ in terms of the size ratio S_R . The ratio of *hatched* and *white* areas under the curve determines the probability of finding a geometrically shielded element at the crack front

The basic idea of the statistical approach, first introduced in [200], lies in an assumption that the microstructural elements can be simply divided into two main categories of low and high S_R . It means that the low S_R part of the probability density function does not influence the shielding phenomenon that is controlled by the high S_R part. This is clearly seen in Figure 2.10, where the area under the probability curve is divided into two parts. Only elements falling into the hatched part contribute to the shielding effect at the crack front. The S_R value determining the boundary between both parts is denoted by S_{Rc} . The two-part concept is introduced for the sake of both clarity and simplicity because, in fact, some transient range must exist. The S_{Rc} value is expected to vary, for example, with the impurity concentration at grain boundaries in a particular material: Because of generally higher probability

of intergranular cracking, the higher the impurity concentration the lower S_{Rc} value is to be assumed. Therefore, this value is to be considered as a free (fitting) parameter in the statistical analysis. Nevertheless, it should lie somewhere within the transient range $S_{Rc} \in (0.2, 1.0)$.

Denoting the probability density function $p(S_R)$, the relative length of the crack front contributing to GIS can be expressed as

$$\eta = \int_{S_{Rc}}^{\infty} S_R p(S_R) dS_R.$$

In other words, the parameter η means the probability of finding a shielded element at the crack front. This statistical parameter is suggested to be a suitable measure of the GIS efficiency and will be used in further analysis. For a particular material, the value of η can be calculated when determining both the yield stress σ_y from the tensile test (in order to estimate r_p according to Equation 2.21) and the statistical distribution of d from the metallographic sample. Fortunately, the two-parameter (ξ, S_{Rm}) Weibull distribution, where $\xi \approx 2.2$, can be successfully used for all engineering materials [200, 201]. Consequently, one can easily show [11, 204] that the parameter η can be estimated on the basis of the yield stress and the mean grain size only:

$$\eta = \exp \left[- \left(\frac{0.886 r_p}{d_m} \right)^{2.2} \right]. \quad (2.22)$$

The portion p_t of tortuous intergranular or crystallographic morphology of the fracture surface can be experimentally determined by using SEM. Indeed, such morphology is clearly different from that of rather straight transgranular facets (quasi-cleavage or ductile dimples). The tortuous part can also be distinguished by topographical methods utilizing various roughness parameters (see Section 3.1 in more detail). Note that, according to the Cavallery principle [201], the area-based value of p_t is equal to the tortuous portion of crack front. As shown above, however, this portion can also be assessed by setting $p_t = \eta$. Let us assume the proportional rule for a mix of the tortuous and straight morphology, and note that the probability of finding the tortuous element of the crack front (which produces shielding) is equal to η . Then the following modification of Equation 2.15 can be utilized:

$$K_{Ici} = \left[1 - \eta + \eta \left(\left(\frac{\bar{g}_{eff,r}}{R_A} \right)^{1/2} (1 - A_b) + 0.5 A_b \right) \right] K_{Ic}. \quad (2.23)$$

Obviously, Equation 2.23 reduces to Equation 2.15 for $\eta = 1$ (pure brittle mode, GIS along the whole crack front), to Equation 2.10 for $\eta = 1$ and $A_b = 0$ (GIS along the whole crack front, no branching) or to the identity

$K_{Ici} = K_{Ic}$ for $\eta = 0$ (pure quasi-cleavage and/or ductile mode, no GIS). The term in the square brackets is called the static shielding factor [168,171].

2.2.2 Anomalous Fracture Behaviour of Ultra-high-strength Steels

An interesting application example of the statistical approach is a quantitative interpretation of the peculiar fracture behaviour of ultra-high-strength low-alloy (UHSLA) steels. During the 1970s and 1980s, many authors (e.g., [193,205–208]) reported an unexpected increase in fracture toughness with increasing prior austenite grain size (or austenitizing temperature). This is clearly documented by the experimental data of various authors in Figure 2.11, where the mean prior austenite grain size is varied over a wide range $d_m \in \langle 5, 265 \rangle \mu\text{m}$. On the other hand, the impact absorbed energy, as expected, dramatically decreased as shown in Figure 2.12 for the US military 300M steel (AISI 4340 with enhanced silicon content). Such contradictory behaviour is rather exceptional since values of fracture toughness and absorbed energy are usually well correlated [209].

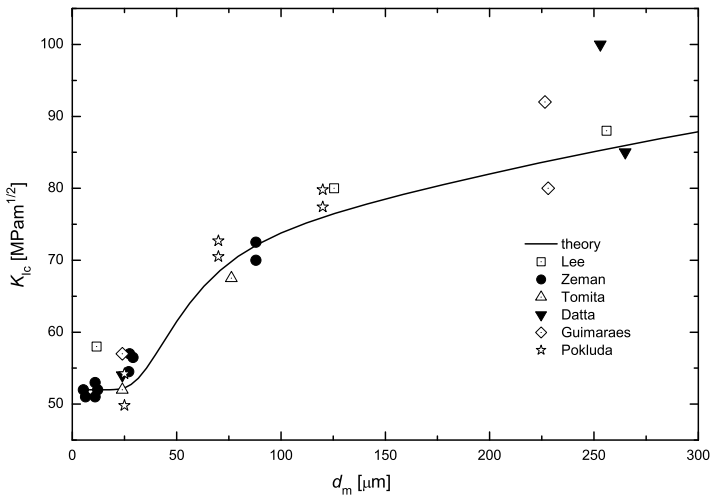


Figure 2.11 Fracture toughness of UHSLA steels as a function of the mean prior austenite grain size d_m . Reprinted with permission from John Wiley & Sons, Inc. (see page 265)

This anomalous behaviour could be explained in a satisfactory manner only after recognizing the difference in fracture modes between fine- and coarse-grained steel grades [210]. While the fine-grained samples exhibited a transgranular dimple fracture morphology, the coarse-grained ones fractured

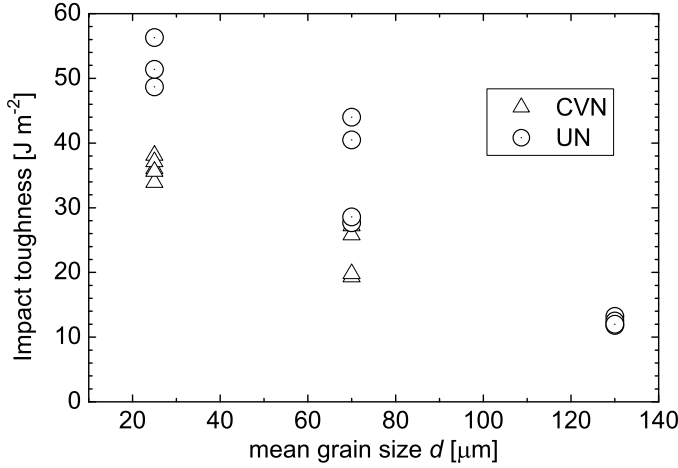
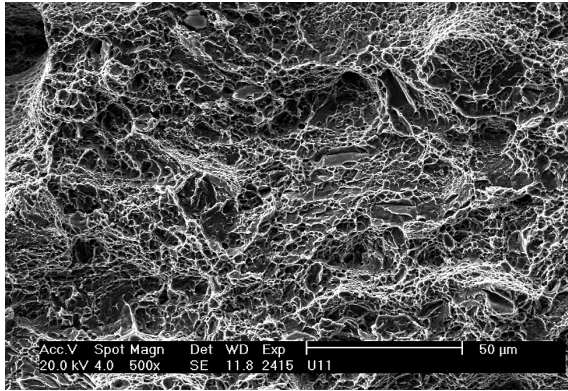


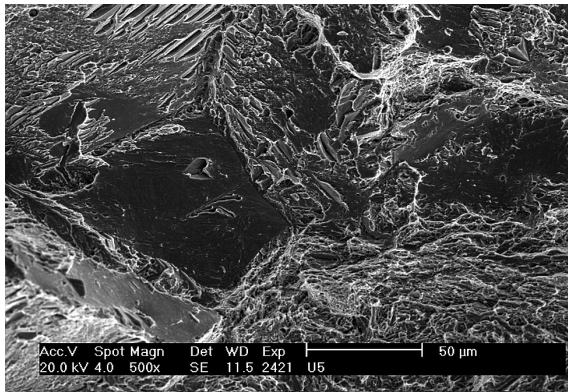
Figure 2.12 Experimental data of the absorbed impact energy in dependence on the mean prior austenite grain size

by intergranular decohesion along prior austenite grain boundaries as documented in Figure 2.13 for the 300M steel. Thus, during the measurement of fracture toughness K_{Ic} , the short stable stage of intergranular crack growth in coarse grained specimens was accompanied by a high level of GIS at the fatigue pre-crack tip. However, the first models [210–212] that attempted to estimate quantitatively the GIS level were only partially successful. The reasons were their two-dimensional and deterministic characters. Only the subsequent, statistically based approaches [168, 213] have led to very reasonable agreement between the theory and experiment. The statistical parameter was determined using Equation 2.22 and the fracture toughness K_{Ic} was assessed according to Equations 2.18 and 2.23 ($A_b = 0$). Nearly the same value of the yield stress was measured for all microstructures since this value is controlled by the martensitic matrix (not by the prior austenite grain size). Thus, $\sigma_y = 1500 \text{ MPa}$ and $S_{Rc} = 0.5$ were considered in the calculations of GIS. The computed values of η are plotted as a function of the mean austenite grain size d_m in Figure 2.14. This function reproduces very well the fraction of intergranular morphology of samples with different mean grain size. In particular, specimens having $d_m < 20 \mu\text{m}$ fractured in a pure transgranular dimple mode, whereas for those of $d_m > 150 \mu\text{m}$ the fracture was fully intergranular.

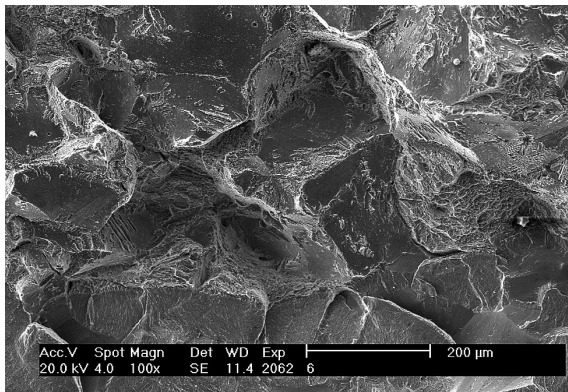
The characteristic periodicities λ_{pl} and λ_{pp} in the pyramidal model were identified with the mean austenite grain size and $R_A = 1.6$ was used as a typical value for intergranular fracture surfaces [214]. The identity $K_{Ici} = 52 \text{ MPa m}^{1/2}$ that corresponds to the fracture toughness of steels with finest grains (no GIS) was accepted for all steel grades. Indeed, owing to the extreme purity of UHSLA steels, the intrinsic fracture toughness associated with both



(a)



(b)



(c)

Figure 2.13 Fracture surface morphology of three grades of 300M steel: (a) transgranular ($d_m = 20\ \mu\text{m}$), (b) mixed trans-intergranular ($d_m = 70\ \mu\text{m}$), and (c) intergranular ($d_m = 120\ \mu\text{m}$). Reprinted with permission from John Wiley & Sons, Inc. (see page 265)

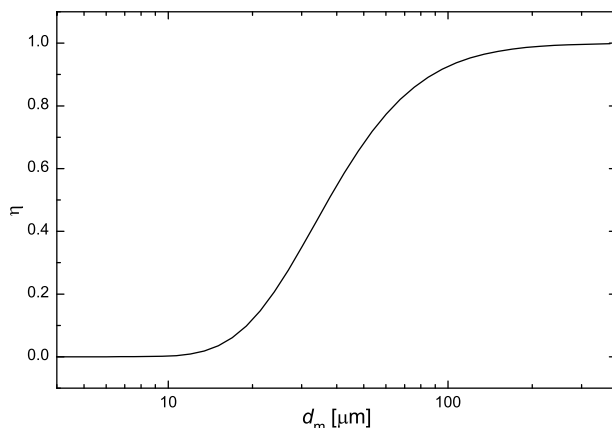


Figure 2.14 Statistical parameter η as a function of the mean grain size d_m

the intergranular decohesion and the fine dimple fracture must be nearly equal. Finally, the dependence of the K_{Ic} values on d_m could be predicted by using the pyramidal approximation according to Equations 2.16, 2.17, 2.18 and 2.23. The result is shown in Figure 2.11 by the full curve. The agreement between theory and experiment is very satisfactory in spite of the fact that only two fitting parameters S_{Rc} , K_{Ici} of physically plausible values were used in this analysis ($A_b = 0$). For the coarsest grades, however, the theoretical curve lies slightly below the experimental data that exhibit the highest scatter. This can be explained by the fact that branching of some of the intergranular crack front segments was not taken into account in the theoretical analysis. As can be seen from Equation 2.23, the branching term might be responsible for the slight difference between theory and experiment in the pure intergranular region.

Let us emphasize that the fracture mechanism in K_{Ic} specimens was quite different from that in the notched specimens used in the impact tests for the measurement of absorbed energy. In the latter case the crack had to be first initiated at the notch root. Therefore, the initiation energy represented a substantial portion of the total absorbed energy. This energy could be well correlated with an extent of shear (stretch) zones adjacent to notches that were clearly identified on the fracture surfaces of all specimens. These zones indicate areas, where the crack was initiated by ductile fracture accompanied by long-range shear coalescence of microvoids with the notch root (see Section 2.3). The shear zones in the coarse-grained specimens were found to be very narrow (and the related energy consumption very low) in comparison to those in fine-grained samples, as documented in Figures 2.15 and 2.16. This phenomenon can be understood in terms of a capability of local microcrack initiation at inclusions or grain (phase) boundaries. Indeed, the local microdefect (microvoid) nucleation assisted by high local stresses ahead of

long dislocation pile-ups in large grains must be much easier, thus reducing the average fracture strain within the notch plastic zone.

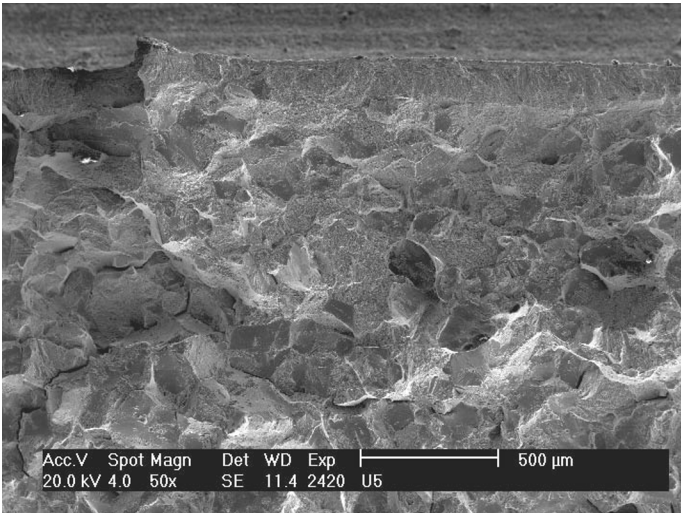


Figure 2.15 The narrow crack-initiation shear zone at the notch (*at the top*) in the coarse-grained sample

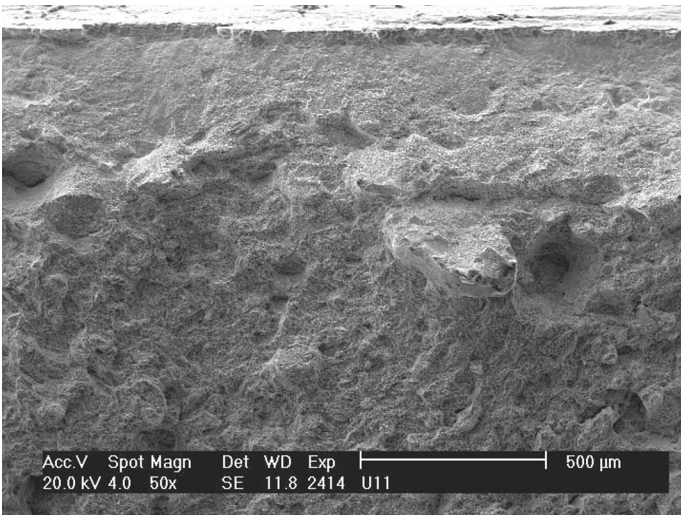


Figure 2.16 The wide crack-initiation shear zone at the notch (*at the top*) in the fine-grained sample

It should be finally noted that an improvement in fracture toughness caused by microstructure coarsening as discussed above is usually associated with a significant decrease in most other mechanical properties [168]. Nevertheless, the increase in an extrinsic component is not necessarily always accompanied by such a detrimental effect. For example, duplex ferrite-austenite microstructures possess extremely high components of GIS while exhibiting other very good mechanical properties (see Section 3.2).

2.2.3 Mixed Intergranular and Cleavage Fracture of Phosphorus-doped Fe-2.3%V Alloy

It is well known that grain boundary segregation of phosphorus, tin and antimony can lead to intergranular fracture. However, finding a quantitative relationship between the segregation level and fracture toughness (or surface energy) constitutes a very difficult task. Therefore, an extended study of fracture behaviour and grain boundary chemistry in an Fe-3%Si based alloy, which contained traces of phosphorus, has recently been performed [215]. Even though this study provided us with unambiguous results, the data may have suffered from the fact that both silicon and phosphorus segregate to the grain boundaries and reduce the cohesion of the material [160]. Additionally, due to repulsive interaction between phosphorus and silicon, a complex segregation behaviour occurs (i.e., enrichment with phosphorus but depletion of silicon) [216]. Many straightforward results in this respect could be obtained by measurement of phosphorus segregation and fracture behaviour in phosphorus-doped iron or in a ferrous alloy containing an element indifferent to phosphorus segregation. Therefore, the phosphorus-doped Fe-2wt%V base alloy was selected [217]. Here, the austenite γ -phase was fully avoided and the system remained bcc up to the congruent melting point. This made it possible to grow bicrystals directly from the melt. Moreover, vanadium does not affect the grain boundary cohesion significantly and, in addition, its segregation is expected to be rather low. From this point of view, one may consider this alloy as a pseudobinary Fe-P system.

Polycrystals of an Fe-2.3wt%V-0.12wt%P alloy were prepared by hot rolling of the vacuum cast master alloy between 1070 K and 1370 K annealing at 973 K for 1 h so that an average grain size of 0.2 mm was achieved. The notched samples for fracture testing were annealed for interfacial segregation at 1073 K (24 h), 973 K (48 h), 873 K (72 h) and 773 K (168 h). Annealed samples were deformed in three-point bending at room temperature using the Zwick Z 020 testing machine. Because the validity of small-scale yielding was not fulfilled for all samples, the fracture toughness K_{Jc} was evaluated according to ASTM E399-72 procedure. The data are listed in Table 2.3. It should be emphasized that force-displacement curves of all specimens exhibited a short nonlinear part indicating a dislocation-assisted stable crack

Micromechanisms of Fracture and Fatigue

In a Multi-scale Context

Pokluda, J.; Šandera, P.

2010, XIII, 293 p., Hardcover

ISBN: 978-1-84996-265-0